Analysis Of The Ghosts From The Earthshine Experiment: DTU Special Course

DMI Report 25-06

January 2025

Contents

Approval

This report presents the work carried out during a special course for the BSc in Earth and Space Physics and Engineering education in 2024. This project is a collaboration with the Danish Meteorological Institute DMI.

The project has been carried out under the direct supervision of Mathias Benn and Peter Thejll. I would like to express my gratitude to Mathias Benn and Peter Thejll for their guidance and assistance during this process.

Dansk Abstract

Denne rapport har til formål at undersøge de observerede refleksioner i billederne fra Earthshine eksperimentet fra Huginn missionen, hvor månen blev fotograferet fra den internationale rumstation. Rapportens primære fokus er det optiske fænomen "ghosting", der skyldes refleksioner mellem overflader i det optiske system. Disse artefakter har stor indflydelse på halo profilerne målt i Earthshine eksperimentet og ønskes derfor undersøgt. I analysen vil bølgelængde afhængighed i forbindelse med placering af reflekserne, pixel intensitet samt symmetri undersøges. Derudover undersøges hypotesen om diffraktions-lignende adfærd, selvom årsagen til dette forbliver usikkert. Som en del af analysen simuleres det optiske system ved brug af ray tracing software for indblik i samspillet mellem de optiske elementer og i hvilke refleksioner opstår. Resultaterne muliggør forbedringer af eksperimentet og som et vigtigt redskab til at minimere ghosting i lignende eksperimenter.

Abstract

This report investigates reflections observed in the images of the Earthshine experiment conducted as part of the Huginn mission, which involved photographing the Moon from the International Space Station. This study focuses on "ghosting" artifacts, caused by internal reflections within the optical system, which interfered with measurements of the halo profiles. By analyzing wavelength-dependent ghost displacement, intensity, and their symmetrical patterns, the study attributes the artifacts to diffraction-like effects, though their exact source remains uncertain. Ray tracing simulations and analysis of the optical setup provide insights into ghosting mechanisms, guiding future improvements for minimizing artifacts in similar experiments.

Acknowledgements

1   Introduction

The Earthshine experiment was a part of the Danish astronaut Andreas Mogensen's Huginn mission. It was a collaboration between the Danish Meteorological Institute (DMI) and the Department of Space Research and Technology at the Technical University of Denmark (DTU Space). During his time on the International Space Station (ISS), Andreas Mogensen photographed the Moon close to the New Moon phase through the windows of the Cupola module. These images were collected approximately one month apart, resulting in more than 4500 images. As a part of the experiment, DMI and ESA invited the public to participate by taking pictures of the Moon [1].

The Experiment aimed to investigate to what extent the scattering of light produced by the atmosphere could be reduced when observing the Moon outside Earth's atmosphere. Earthshine refers to the dim illumination of the Moon's surface caused by sunlight reflected off Earth. This method, known as the Earthshine method, measures Earth's reflectivity, or albedo, which is essential for understanding Earth's climate. By using the Moon as a projection screen, the amount of light reflected from the Moon can be used to calculate how much sunlight is reflected by Earth, as the ratio of the intensity of the Moon's bright side and dark side, from now on noted as BS and DS. Albedo measurements are greatly affected by Mie scattering caused by the atmosphere, along with aperture diffraction from the optics, which lowers important contrasts used to estimate the albedo.

The experiment was the first to be conducted outside Earth's atmosphere, providing a unique opportunity to separate the effects of Mie scattering, from aperture diffraction, which can introduce noise and errors into Earthshine measurements. The primary objective was to analyze differences in the halo profiles of the Moon images from the ISS compared to those captured from Earth. The results could also provide useful knowledge for the Earthshine space telescope JULIET developed at DTU Space in collaboration with IRS.

A significant challenge in analyzing the Earthshine experiment's images was the presence of reflections of the Moon or ghosting. These artifacts, caused by reflections within the optical system, appeared as symmetrical images around the Moon's bright side. Because these ghosts overlapped with the halo profiles being studied, they decreased the accuracy of the measured halo profiles. The ghost artifacts appeared to exhibit dispersive behavior, complicating the analysis even further.

Understanding the characteristics of ghosting is essential for mitigating its impact on data analysis. This study aims to identify the origin of the ghosting artifacts within the optical system and determine their influence on the halo profiles. The results of this study could inform strategies for minimizing ghosting in future experimental setups, whether through improved optical design or post-processing techniques.

2 Theory

2.1 Imaging By an Optical System

The process of capturing images involves three main components: energy from the object of interest, an optical system that focuses this energy, and a sensor that measures the intensity of the focused energy [2].

The mechanism of classical imaging is central projection, where points in the object space are mapped to corresponding points in the image space by the optical system [3].
The optical system directs the lights towards the sensor to produce a sharp image of the object. Rays from the object intersect at the focal points F, and the distance between the lens center O and F is called the focal length f. The thin lens equation expresses the relationship between the distances involved:

$$\frac{1}{g} + \frac{1}{b} = \frac{1}{f} \tag{1}$$

Where g is the distance between the object and the lens, b is the distance between the image and lens, and f is the focal length. When the system fails to produce an ideal image, aberrations occur, such as chromatic aberration, where lenses fail to focus all colors at the same point due to wavelength-dependent refraction. This results in blurring and color fringing as the lens behaves like a prism, bending light differently for each wavelength

2.2 The Camera

The sensor in a digital camera is a critical component that converts photons into measurable voltage. Before capturing an image, the sensor's cells are cleared to remove residual charges [4]. The aperture controls the amount of light entering the camera, influencing both brightness and the field of view. The shutter determines the exposure time, regulating how much light reaches the sensor. Long exposure times allow more light to enter but risk overexposure, while short times may cause underexposure, both cases result in loss of linearity.

The sensor itself is a semiconductor array of photodiodes that measure photon intensity and convert it into voltage. On top of each pixel sits a microlens to enhance light-capturing abilities and focus the light on the light-sensitive area [5].
Color information is captured via a color filter array (CFA), which uses band-pass filters for red, green, and blue wavelengths. Each CFA unit typically contains two green filters, reflecting the human eye's sensitivity to green light. The camera reconstructs the color information from the CFA by interpolation in a process noted as demosaicing [2]. Modern cameras also include optical filters, such as IR and UV cut filters to block out unwanted wavelengths. These are often included in the Optical Low Pass Filter (OLPF) or Anti-Aliasing filter to reduce moiré patterns and high-frequency image information. The filters are typically placed between the sensor and the lens [6].

2.3 Ghost Images and Stray Light

In optics, ghost images are faint secondary images caused by internal reflections within an optical system. Ghosts often appear out of focus and can distort the main image. If the ghost is focused on the image plane, the ghost takes the form of the source.

The relative intensity of the ghosts depends on the number of light reflections and the reflectivity of the surfaces. The intensity decreases rapidly with the number of bounces and the likelihood of ghosting increases with the number of lens elements. To mitigate this, lens manufacturers apply anti-reflection coatings to optical surfaces. Reflections introduce distortions by chromatic aberrations. Sasián [3] identifies the following causes of ghost images:

Total Internal Reflections ghosts, occur due to a combination of a single Fresnel reflection and total internal reflection within the lens. This type of ghosting produces bright artifacts, as the light only experiences losses from one Fresnel reflection.

Parallel flat or concentric lens surfaces can also cause ghosting. In this case, light reflects off the rear surface of an optical element, then off the front surface, following the same path as the original light. This creates a ghost image that is in focus with the main image.

Narcissus retro-reflection ghost is the type of ghosting that occurs when light reflects off the sensor (or image plane) and is then reflected back towards the sensor by another surface. Since the reflected light followed the same path as the original, the resulting ghost image is sharp and focused. This is also described by Brauers and Aach [7]. Reflections occurring between the sensor and the optical bandpass filter result in ghosting. Reflections between the optical filters and lens exit are blurred and low frequency, this is also noted as glare.

2.4 Dispersion

Dispersion occurs when light of different wavelengths is refracted at different angles due to different refractive indices. In normal dispersion, shorter wavelengths (blue) are refracted more than longer wavelengths (red). Dispersion causes chromatic aberrations, leading to color separation and image distortions. In comparison, angular dispersion from diffraction gratings is due to interference at each wavelength. longer wavelengths are diffracted more than shorter wavelengths.

2.5 Diffraction Grating

Diffraction is defined as "any deviation from geometrical optics that results from the obstruction of a wavefront of light" [8]. For a single slit, the angle of diffraction is given by:

$$sin\ \theta = \frac{m\lambda}{b} \qquad (2)$$

Where b is the slit width, λ is the wavelength of the light and m is the diffraction order. The angle of diffraction can also be related to the physical geometry of the diffraction pattern by:

$$tan\,\theta = \frac{y}{L} \tag{3}$$

Where y is the distance between diffraction orders, and L is the distance between the diffraction grating and the imaging surface where the diffraction pattern is observed. When light reflects off the sensor and interacts with nearby filters, diffraction patterns can arise due to retro-reflection. This behavior is modeled as:

$$L = \frac{y}{2tan\,\theta} \tag{4}$$

Here, L represents the effective distance between the sensor and reflective components, such as IR cut filters, accounting for the light's double traversal path.

This chapter has outlined the principles of imaging, optical system components, and phenomena such as ghosting, dispersion, and diffraction. These foundational concepts are essential for understanding the ghost artifacts observed in Andreas Mogensen's Moon images and their impact on Earthshine experiment analysis.

3 Experimental Setup and Data

The Moon was photographed close to the new Moon phase at Moon-rise through the windows of the Cupola module [1]. The images were collected in a series using bracketing taken 1 month apart, where each image series contained approximately 200 to 500 RAW images. Throughout the experiment, more than 4500 images were collected.

3.1 Experimental Setup

The following is based on information provided by Andreas Mogensen when asked about the experiment.

The camera was mounted onto the windows using a multipurpose bracket to avoid movement. This was implemented after the first session. At length, all light sources within the cupola were covered and light was turned off in adjacent modules. Andreas also states that he used a shroud between the lens and window to shield the camera further. The distance between the window and the lens was kept the same at a few centimeters. This was due to restrictions on the multipurpose bracket and the length of the lens.
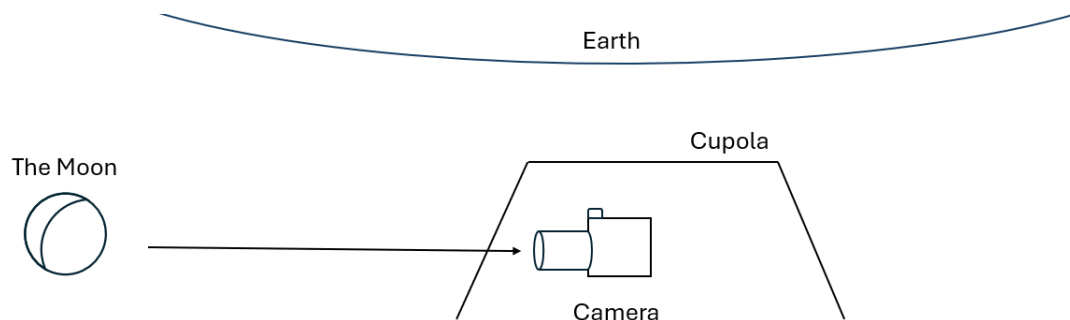
Figure 1: The figure shows a sketch of the experimental setup.

Andreas states that he waited until the Moon was visible before choosing the best window to photograph the Moon through. He then mounted the multipurpose bracket onto the window. Then he photographed the Moon while sometimes tilting the camera either up or down to keep the Moon in the center of the image. The geometry of the Moon's position and the window determined the angle between the window surface and the lens.

3.2 The Windows of Cupola

The Cupola module consists of a total of seven windows, 6 trapezoidal side windows, and one round nadir window parallel to the surface of the Earth. The round nadir window is not considered throughout this report, since only the side windows were used to conduct the images by Andreas Mogensen and later Matthew Dominick.

The measurements of the side windows are:

- Height of the transparent area 40.5 cm

- Length of the short side 40.0 cm

- Length of the long side 64.4 cm

The windows are tilted 30 degrees to a line normal to the surface of the Earth, see Figure 1. Figure 2 shows the composition of the windows of Cupola. Each window consists of four
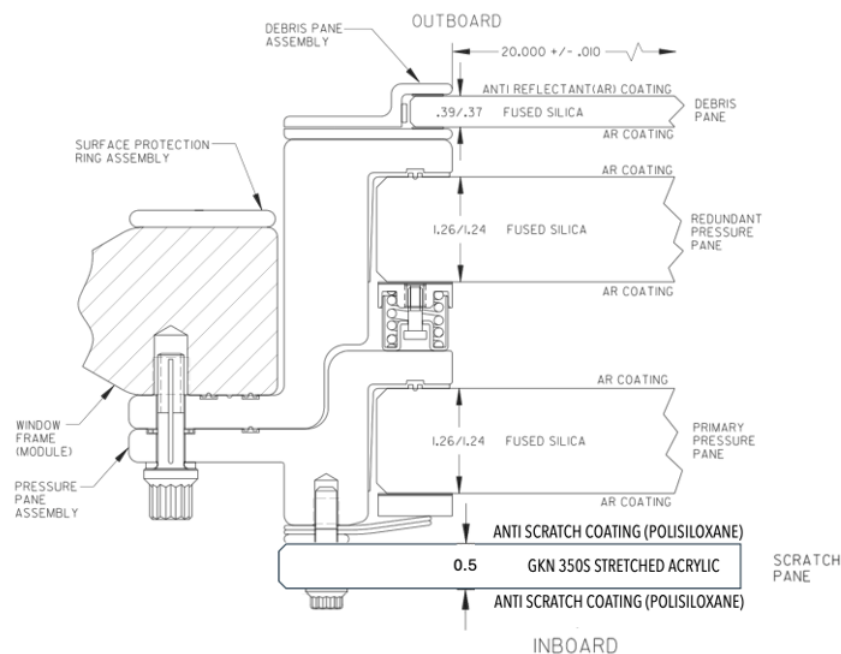
Figure 2: The figure shows the working drawing of the cupola window assembly as the cross-section of the four panes

panes: The outermost pane, the debris pane is composed of fused silica, and each surface is coated with an anti-reflectant (AR) coating and is 0.94 cm thick. The next two panes, the pressure panes are also composed of fused silica and AR coated, the two pressure panes share the same thickness at 3.15 cm. The last and innermost pane is the scratch pane, composed of stretched acrylic and treated with a polysiloxane anti-scratch coating on each side.

Cupola Window Assembly				
Directory	**Material**	**Thickness**	**Coating**	**Coating Material**
Debris Pane	FUSED SILICA	0.94 cm	ANTI REFLECTANT (AR)	MgF2
Pressure Panes	FUSED SILICA	3.15 cm	ANTI REFLECTANT (AR)	MgF2
Scratch Pane	GKN 350S STRETCHED ACRYLIC	1.27 cm	ANTI SCRATCH COATING	POLISILOXANE

Table 1: Cupola window information

It was not possible to obtain the measurements of the spacing between each pane, the following values are therefore suggested widths based on measurements from Figure 2.

Distances Between Panes			
Panes	D Pane - P1 Pane	P1 Pane - P2 Pane	P2 Pane - S Pane
Distance	1.5 cm	3.3 cm	1.55 cm

Table 2: Appriximate distance between each window pane

The following were stated in [9] for the specifics regarding the window design.

- The transmittance SHALL be not less than 60.0 percent for wavelengths between 800 and 450 nanometers.
- All glass window panes SHALL not exhibit warp and bow greater than 0.030 inch per linear foot of glass.
- Specular reflectance from each anti-reflection coated surface, disregarding red−reflector coated surfaces, for 450 to 700 nanometers normally incident light SHALL not exceed 2.0 percent absolute.

These were some of the requirements to ensure the optical quality of the cupola module windows for scientific research.

3.3 The Camera

The images were captured using a Nikon D5 camera with a telephoto lens. The Nikon D5 camera uses a CMOS sensor - Complementary metal−oxide−semiconductor. CMOS sensors consist of individually addressable photodiodes enabling the storage of all pixels at once. Each pixel has individual amplifiers and conversions between photons to charge and charge to voltage.
As mentioned in subsection 2.2, cameras use CFA's for color impression. The Nikon D5 sensor uses a Bayer pattern where the unit cells are organized in the following way:

$$\text{CFA} = \begin{matrix} \textcolor{red}{R} & \textcolor{green}{G} \\ \textcolor{green}{G} & \textcolor{blue}{B} \end{matrix}$$

As mentioned in subsection 2.2, modern camera sensors use microlenses for optimization. Nikon uses a gapless design to capture more incoming light. In addition, each microlens is offset to the pixel underneath, to capture light from oblique incident near the edges of the array [5].

3.4 The Lens

The lens used is a Nikon AF-S Nikkor 400mm f/2.8D IF-ED. It is a telephoto lens, with a max aperture of f/2.8 and a focal length of 400 mm as stated in the name. The physical length of

the lens is 352 mm and the diameter is 160 mm [10]. A telephoto lens is a long-focus lens that has a focal length that is longer than the physical length of the lens.

The lens consists of 11 optical elements arranged in 9 groups. Among these, 3 elements are made from Extra-Low Dispersion (ED) glass, specifically designed to minimize chromatic aberrations. According to Nikon's NIKKOR Lens Glossary, "this low-dispersion ED glass also exhibits anomalous dispersion characteristics, similar to calcium fluoride crystals, effectively minimizing the secondary spectrum" [11].

3.5 Data

The data used in this project, are the original images from the Earthshine experiment of Andreas Mogensens Huginn mission and images by the astronaut Matthew Dominick from the extended experiment. The images are in RAW format, such that no demosaicing has been applied, keeping the measured intensities of each color band untouched. The data type of the images is uint12 (unsigned integer format) meaning the pixel intensity is in the range of $[0; 2^{12} - 1]$ or $[0; 4095]$. The experiment was carried out with specific settings to avoid overexposure to measure the contrast between the BS and the DS of the Moon.

To summarize, this chapter describes the important components of the optical system and how the images were obtained in the experiment.

4 Observations

This chapter illustrates the findings within each image series to group the different observed patterns of ghosts before further analysis. The observations are based on images taken by the ESA astronaut Andreas Mogensen and the NASA astronaut Matthew Dominick.

4.1 Different patterns in placement of ghosts

Figure 3 shows the different observed patterns in the placement of the ghosts occurring in the images from the Earthshine experiment.
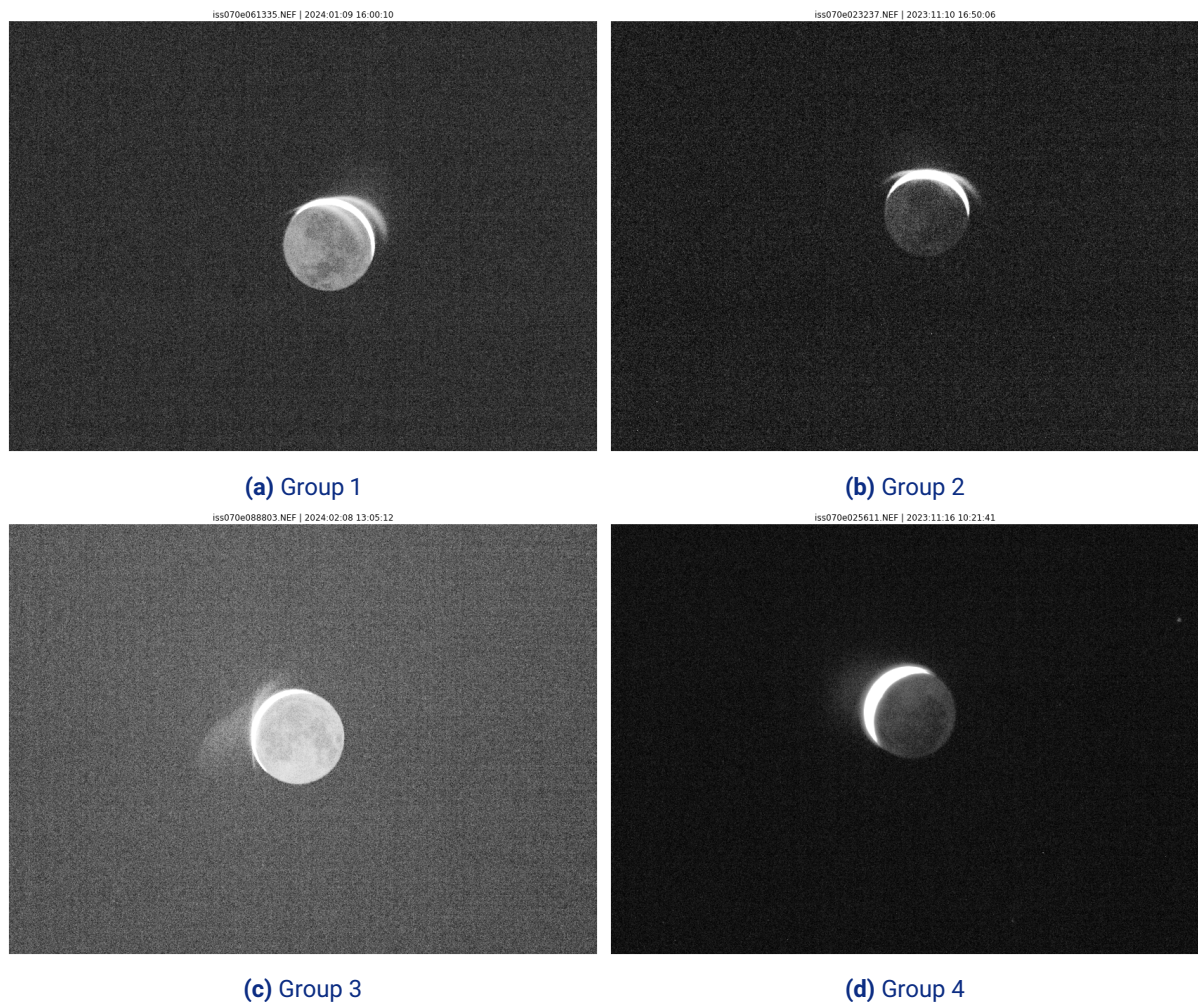

(a) Group 1

(b) Group 2

(c) Group 3

(d) Group 4

Figure 3: The different patterns of ghosts observed.

Group 1

The ghosts are placed on each side of the bright side (BS) of the Moon, one outside and the other on the dark side (DS). The ghosts are symmetrical and intersect the BS far from the

center. See Figure 3a.

A subgroup of this pattern can be seen in Figure 13 in Appendix A, where four aberrations are present within the image. This pattern has only been observed within the GMT155 series taken by astronaut Matthew Dominick.

Group 2

The ghosts are placed symmetrically on each side of the middle of the bright side of the moon. The ghosts are displaced along the horizontal axis, forming an X. See Figure 3b.

Additionally, a change in the placement of the ghost has been observed within the same series. See Figure 14 in Appendix A.

Group 3

The placement of the ghosts is similar to that of Group 1, but the ghost located on the moon's dark side appears more faint than the other. Furthermore, an additional artifact is seen outside of the bright side. See Figure 3c

Group 4

This group has only one visible ghost outside the Moon's bright side. The ghost appears as a diffuse collection of light in contrast to the other groups, the bright side could hide other details. See Figure 3d
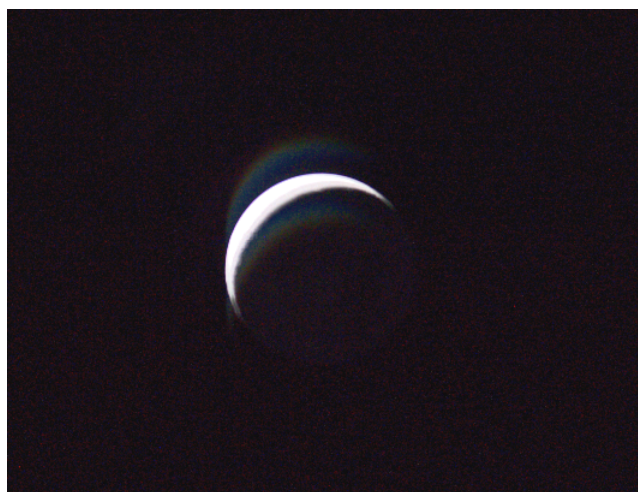
4.2   Ghost profiles

Figure 4: RAW image iss071e160861.NEF was viewed using Shotwell, the image has been manipulated to enhance the appearance of the ghosts.

When viewing the RAW images using an image management application - in this case, Shotwell. The developed JPEG shows a rainbow-like appearance of the ghosts and the

symmetrical placement around the BS. Each ghost is shifted horizontally and vertically according to the array. Both ghosts seem to have the same intensity. Furthermore, the shortest wavelengths are placed closest to the primary object - the bright side of the moon, and the longer wavelengths are furthest away.

To investigate this further, the original RAW image is separated into each color channel of the color filter with the components R, G, G2, and B.

(a) R - band

(b) G - band

(c) G2 - band

(d) B - band
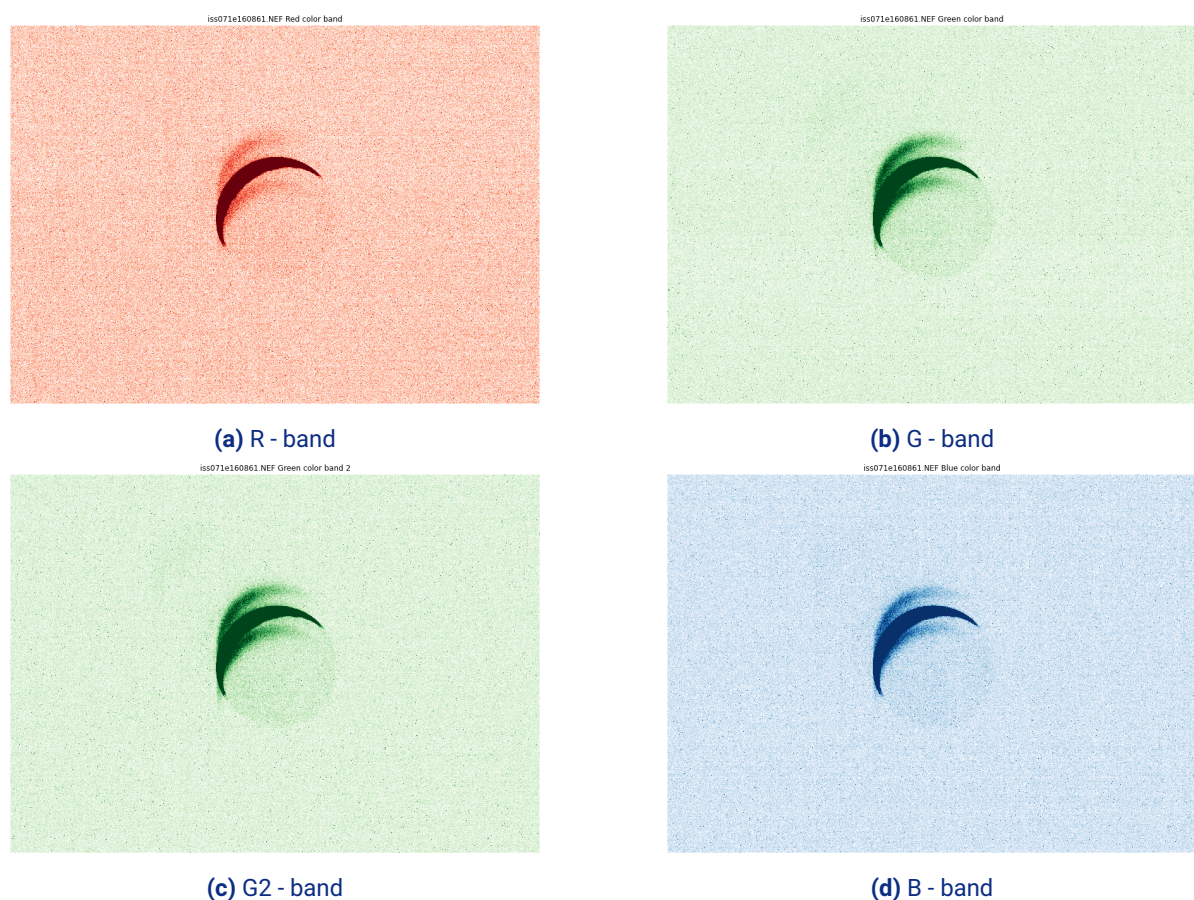
Figure 5: The four color-band images from the RAW image.

By examining each image in Figure 5, it becomes evident that the ghost reflections for each color channel are visibly offset. As interpreted by Shotwell, shorter wavelengths appear closer to the source while longer wavelengths are positioned further away. Additionally, the two green color channels appear identical, as expected since they measure the same wavelength range.

To summarize, this chapter illustrates the initially observed characteristics of the ghosts and divides them into groups categorized by the observed pattern.

5 Method

This study aims to investigate the characteristics of ghost reflections, including their wavelength-dependent displacement and intensity variations, as well as to identify the optical system components responsible for their formation. Key characteristics, such as angular dispersion, are analyzed using a combination of measured pixel intensity profiles and ray tracing simulations.

5.1 Pixel Intensity Profile

To analyze wavelength dependency, the color information in RAW images is leveraged. Pixel intensity profiles are extracted for the red (R), green (G, G2), and blue (B) color bands, enabling a detailed comparison of displacement and intensity differences among the ghosts. The RAW images are processed using 4channels from the LibRaw library [12], which decodes the underlying CFA pattern and produces separate 16-bit TIFF images for each color channel. The G and G2 channels, sensitive to the same wavelengths, are analyzed separately to identify potential errors; significant differences would indicate inconsistencies in the optical path or sensor response. The black subtraction function is turned off when splitting the images into color channels as the background is subtracted later.

Noise Reduction

To improve the Signal-To-Noise Ratio (SNR), multiple images are aligned and combined into an average image for each color band. Alignment is achieved via cross-correlation with a reference image to ensure consistent orientation and positioning. The method reduces noise by a factor of $\sqrt{n}$, where n is the number of images [4].

Images are carefully selected to minimize differences in the positions of the ghosts. In addition, only images with similar exposures are chosen and overexposed images are removed from further analysis. The background is subtracted for each average image assuming uniform intensity across the image. The resulting background-subtracted images are smoothed using a median filter (disk-shaped, radius 1) to reduce salt-and-pepper noise.

Ghost Profiles

Linear pixel intensity profiles are extracted for equal regions in each color band image, to capture the bright side (BS) of the Moon and both ghosts within a single profile. Each profile is obtained using the SciPy 1-D smoothing spline fit function `UnivariateSpline` [13], with a smoothing factor of 55 and focusing on pixels above the background level. For each profile, the 3 highest peak intensities are identified on both sides of the main peak. Assuming the peak intensity of the two ghosts is approximately symmetrical around the BS. Along with the intensities, the position along the profile for each peak is derived. The intensities are expressed relative to the main peak (BS) intensity for each color. At length, Distances are centered at the BS peak, with increasing pixel values on either side.

Angular Dispersion

Angular dispersion is analyzed to investigate wavelength-dependent displacement of ghost reflections, assuming the sensor functions as a diffraction grating.

The measured diffraction angle is determined from the estimated distances between the ghosts and the main peak using (3). The distance L is then approximated using (4), as an estimate for the actual separation between the IR cut filter and the sensor, which was unavailable. The theoretical diffraction angle for the first order, intended for comparison with the measured values, is calculated using (2). This calculation assumes that the slit width of the grating corresponds to the pixel pitch - the spacing between individual pixels.

Since the camera's spectral sensitivity was unavailable, representative wavelengths were selected for each color band. These are $\lambda_R = 625$nm for the red channel, $\lambda_G = 545$nm for the green channel, and $\lambda_B = 450$nm for the blue channel, based on data from [14].

5.2   Ray Tracing

Ray tracing simulations using Zemax OpticStudio are employed to analyze the origins of ghost reflections and stray light within the optical system.

Non-sequential ray tracing is performed based on the experimental setup and optical components, focusing on the Cupola windows. The model is based on the information on the windows described in subsection 3.2. Due to limited data on the camera and lens design, the simulation emphasizes the role of the initial optical elements, such as the Cupola windows, in generating stray light and reflections

The goal of the analysis is to identify components causing the ghost images and assess how dispersion and diffraction effects within the optical system influence the formation and characteristics of the ghosts.

6 Results

This chapter presents the results of the measured ghost profiles and examines the angular dispersion of the diffraction angle based on these profiles. Additionally, a simulation of the Cupola windows is conducted using ray tracing to analyze the behavior of the optical system.

6.1 Ghost Profile

For the analysis of ghost reflections using intensity profiles, images exhibiting the ghost pattern of Group 1 were selected. A pixel intensity profile was extracted from a combined averaged image created from the GMT009 image series, captured by Andreas Mogensen during the Huginn mission. The resulting image, shown in Figure 16, is an average of six aligned images, with each color band aligned to the same reference image.
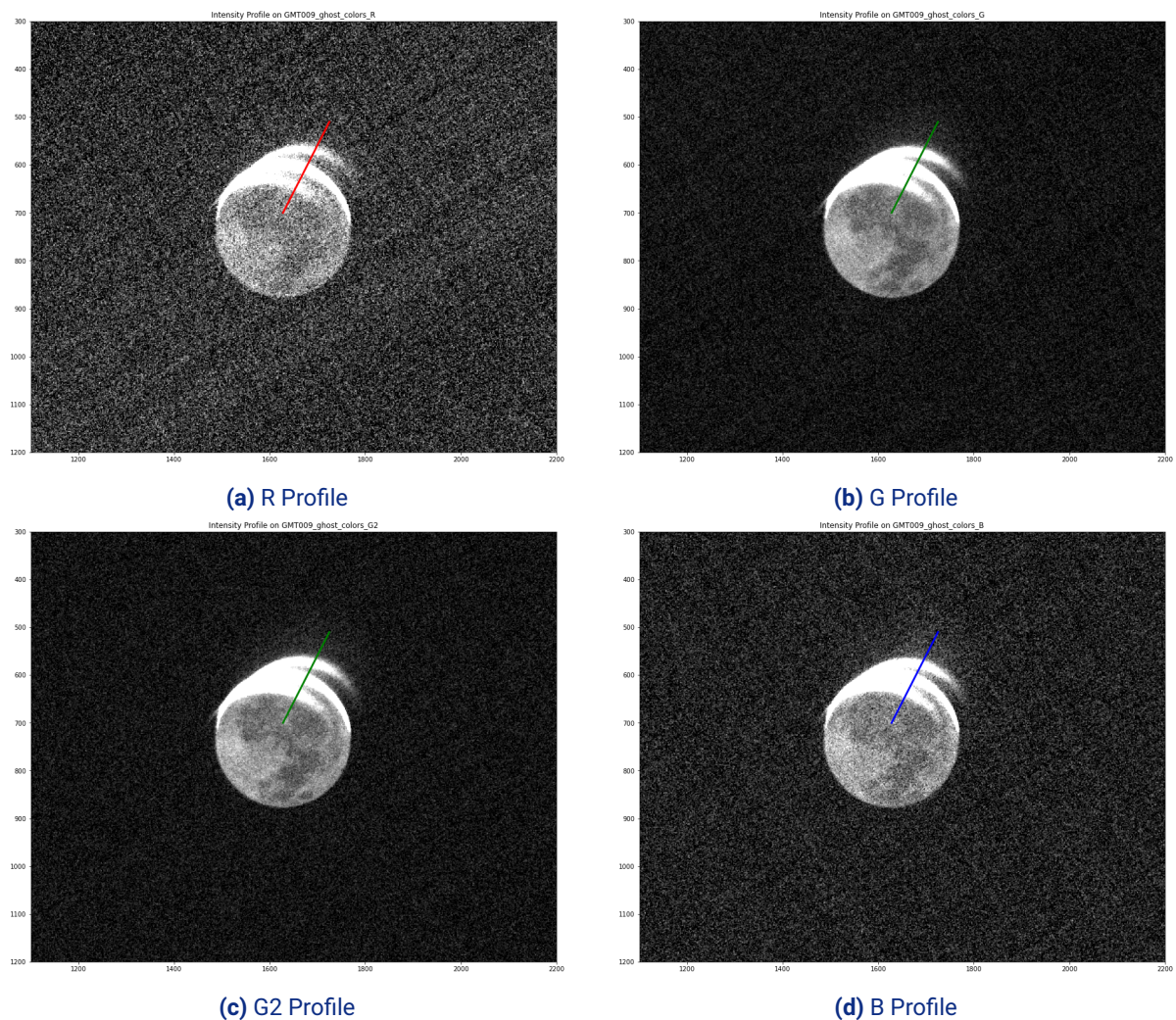

(a) R Profile

(b) G Profile

(c) G2 Profile

(d) B Profile

Figure 6: The figure shows the profile placement on the average image in each color channel, the intensity for each image is stretched for visual enhancement.

The profile was placed in the same position for each color band. The measured intensities and distances along the profile for the ghosts and the BS are shown in Figure 7.
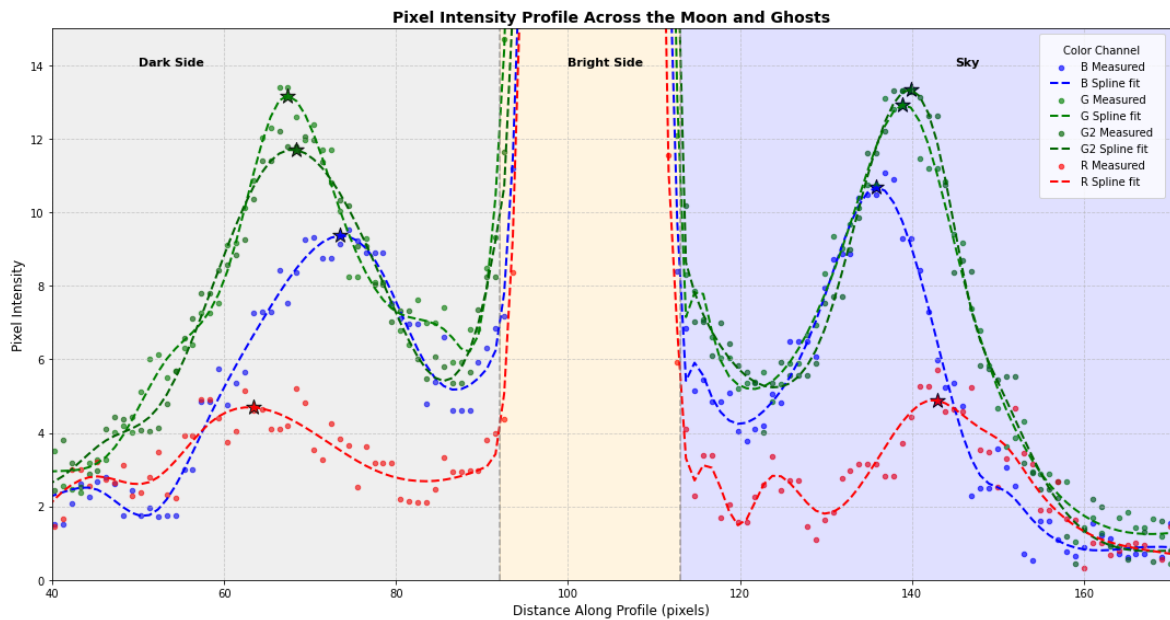

Figure 7: The measured and fitted pixel intensity profile for each color. A star marks the position of each peak of the fitted profile.

Figure 7 shows a symmetrical pattern in the offset between the ghosts to the BS and similar intensities. The measured values for the intensity I and the distance x along the profile from Figure 7 are shown in Table 3

Table 3: Summary of Main and Ghost Peak Properties for Each Color Band

Color	BS Peak x	BS Intensity I	Ghost 1 x	Ghost 1 I	Ghost 2 x	Ghost 2 I
B	106.66	1754.57	73.46	9.37	135.85	10.69
G	106.66	2925.77	67.42	13.18	138.86	12.93
G2	106.66	2894.47	68.43	11.70	139.87	13.34
R	106.66	1442.70	63.39	4.69	142.89	4.89

The position of the main peak (the BS) at $x = 106.66$ pixels remains consistent across all color bands. However, the intensity of the main peak varies by color, with G and G2 exhibiting the highest intensities and R the lowest. It is important to note that these intensities were measured after background subtraction. The ghost intensities are slightly above the background level, where $I_{sky} = 0$.

Next, the intensities and distances were normalized relative to the intensity of the main peak. By setting the BS peak position to $x = 0$, the normalized intensities for each color are represented as I/I_0. The normalized values for the innermost ghost are shown in Figure 8, with the corresponding data presented in Table 4.
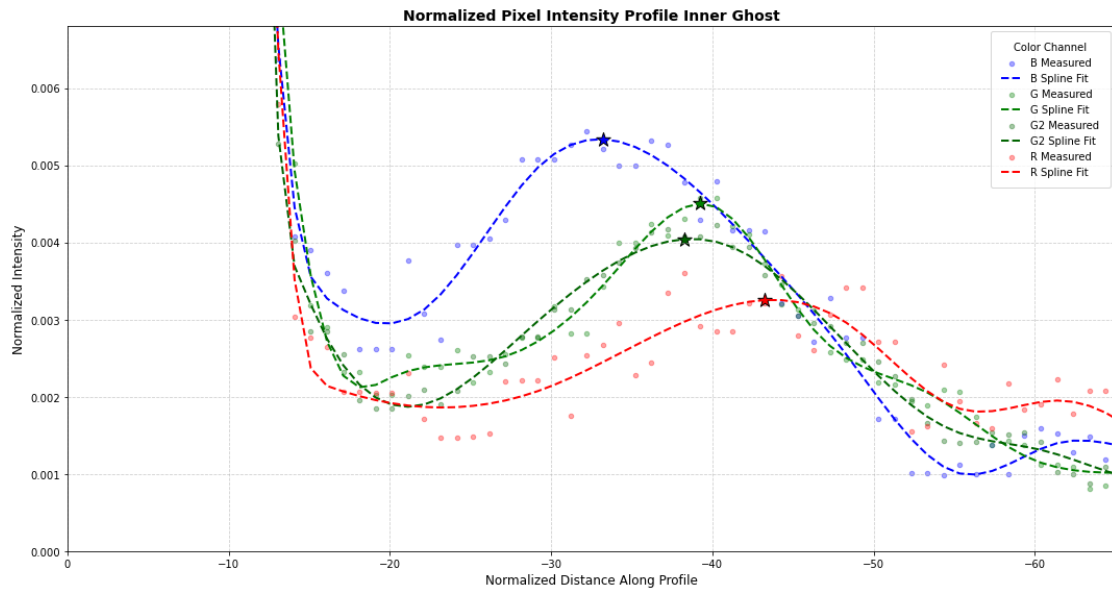

Figure 8: Normalized intensity profiles of the innermost ghost - the one place on the DS.

Inner Ghost		
Color	**Relative Intensity [I/I_0]**	**Distance [pixels]**
R	0.0033	-43.27
G	0.0045	-39.24
G2	0.0040	-38.24
B	0.0053	-33.21

Table 4: The table shows estimated distances and relative intensities. The distances are given in pixels, and the sign relates to the side of the main peak.

An offset between the colors is observed, where the peaks of the red and blue bands are approximately 10 pixels apart - with the green positioned between them. In contrast, the main peak for the BS was the same for all colors. Notably, the Blue band exhibits the highest relative intensity compared to the others, despite the two green color bands having the highest measured intensities of the BS.

The normalized intensities and distances for the outermost ghost are shown in Figure 9 and the measured values in Table 5
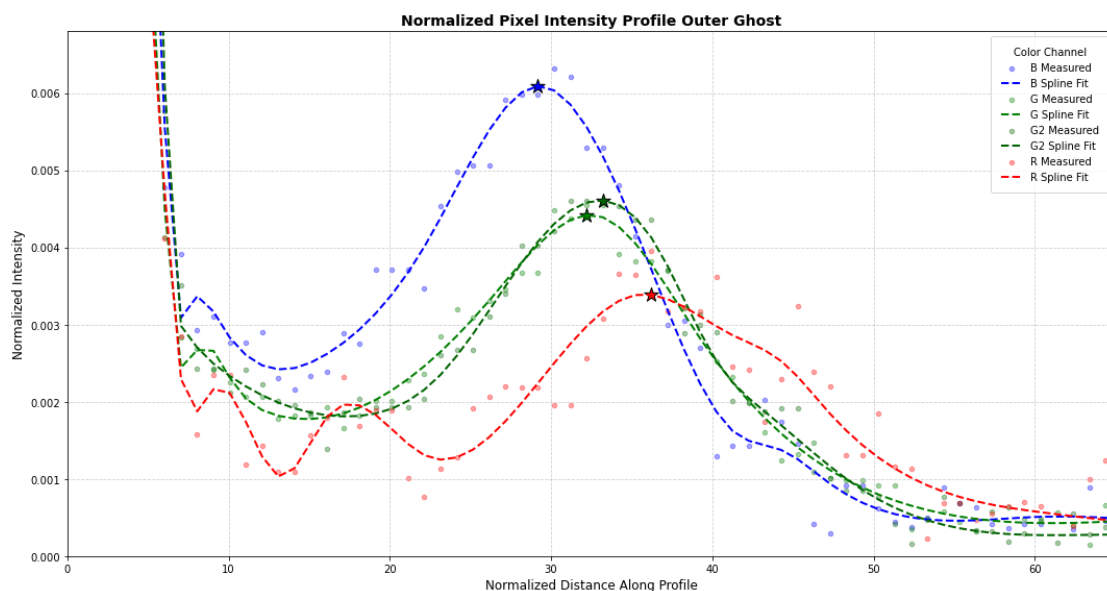

Figure 9: Normalized intensity profiles of the outermost ghost - the one placed outside of the BS.

Outer Ghost		
Color	**Relative Intensity [I/I_0]**	**Distance [pixels]**
R	0.0034	36.23
G	0.0044	32.20
G2	0.0046	33.21
B	0.0061	29.18

Table 5: The table shows estimated distances and relative intensities. The distances are given in pixels, and the sign relates to the side of the main peak.

A similar offset between the colors is shown, where the peaks of the red and blue bands are approximately 7 pixels apart. The Blue band exhibits the highest relative intensity compared to the others, the same as for the first ghost.

The estimated pixel intensities and distances of the ghosts appear to follow a consistent wavelength-dependent behavior. To further analyze this, the measured distances along the profile for each ghost were compared to the expected diffraction assuming the sensor functions as a diffraction grating. Since the exact distance between the sensor and the IR cut filter was unavailable, an estimated value was calculated using the diffraction angle and the measured distances between the ghosts and the main peak. The mean distance L was determined to be $L = 1.35mm$ with a standard deviation of $\sigma = 0.12mm$.

Figure 10 shows the diffraction angle as a function of wavelength based on the measured positions of the ghosts along the profile. The measured positions of the ghost peaks are symmetrical about the main peak (the black dot) at the center.
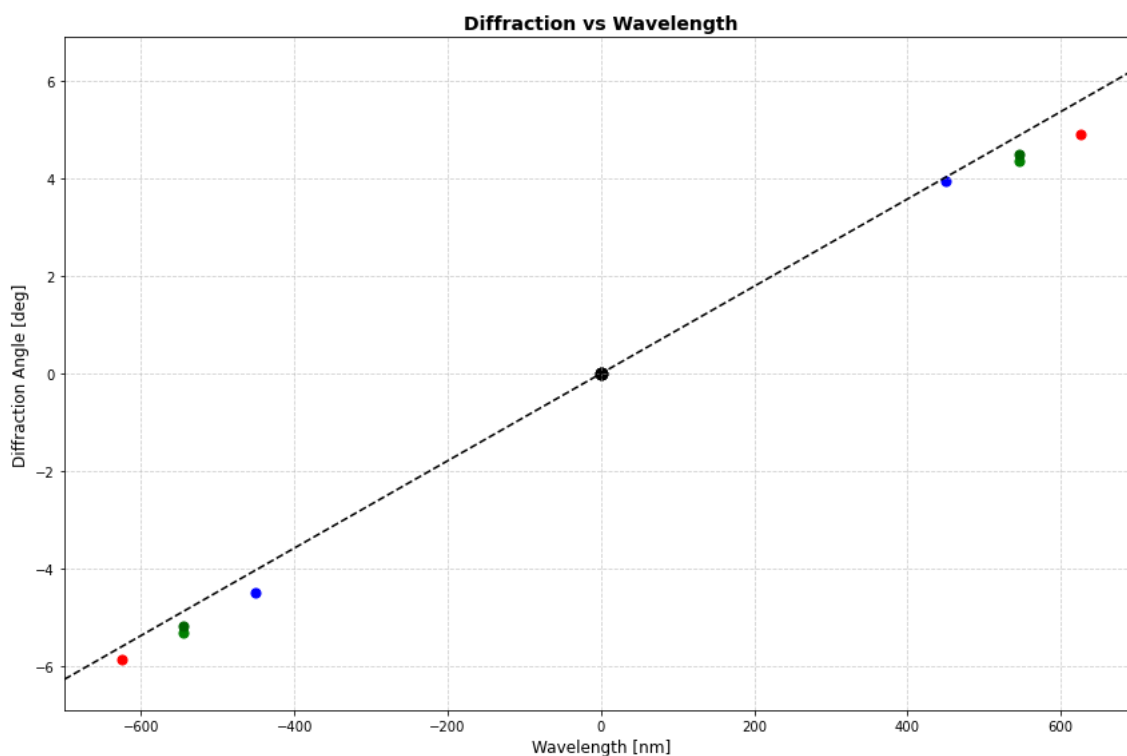

Figure 10: The figure shows the expected diffraction angle from the sensor (the black line) and the measured diffraction for the ghosts (the colored points).

Table 6 and Table 7 shows the theoretical and estimated diffraction angles along the measured positions for inner and outer ghost in each color band. Deviations between theoretical and measured values are observed, particularly in the measured distances, which tend to be slightly larger for the inner ghosts and smaller for the outer ghosts.

Table 6: Comparison of Theoretical and Measured Angles in [deg] and Distances in [pixels] for Inner Ghost

	Theoretical Angle	Measured Angle	Theoretical Distance	Measured Distance
B	-4.0256	-4.4993	-29.6986	-33.2068
G	-4.8774	-5.3130	-36.0100	-39.2444
G2	-4.8774	-5.1776	-36.0100	-38.2381
R	-5.5955	-5.8544	-41.3433	-43.2694

Table 7: Comparison of Theoretical and Measured Angles in [deg] and Distances in [pixels] for Outer Ghost

	Theoretical Angle	Measured Angle	Theoretical Distance	Measured Distance
B	4.0256	3.9558	29.6986	29.1817
G	4.8774	4.3635	36.0100	32.2005
G2	4.8774	4.4993	36.0100	33.2068
R	5.5955	4.9064	41.3433	36.2256

6.2 Zemax

The properties of the windows as part of the optical system were also investigated. An analysis of potential stray light produced by reflections between each surface for the different window panes was obtained using Zemax. The result is shown in Figure 11:
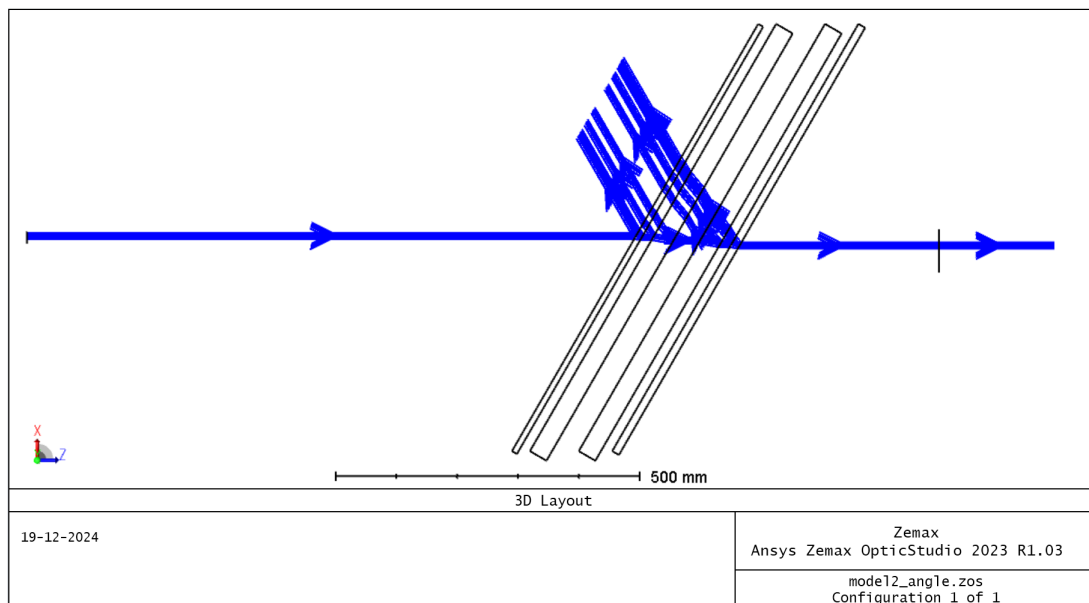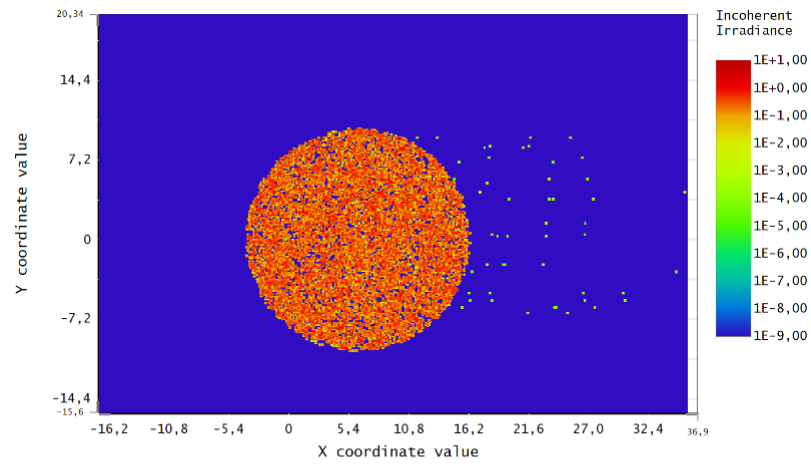

Figure 11: The figure shows the cross-section of the 3D model of the windows and the rays that are used for analysis originating from the source on the left-hand side. The rays are measured by a detector placed on the right-hand side of the system.

The simulation shows the interactions between the incoming light from a source resembling the Moon and each window pane. The arrows show the direction of propagation for each ray. The model was based on the specifics described in subsection 3.2 assuming the light was incident on the 30-degree tilted window panes. Figure 11 shows that reflections occur at several surfaces in the system. The detected rays viewed by the sensor placed on the right side in the model are shown in Figure 12.

Figure 12: The figure shows the recorded light rays on the detector.

The simulation revealed stray light seen on the right side of the object in Figure 12. The intensity of the diffuse reflection is approximately in the range $[10^{-3}; 10^{-5}]$ of the main object. The simulation used 10000 analysis rays and allowed polarization and scattering at each object. As seen in Figure 11, light is reflected back toward space at several window surfaces. The runtime of the simulation was approximately 8 seconds.

7 Discussion

In this chapter, the findings of the analysis are discussed in detail by interpreting the results and possible errors.

7.1 Ghost Behavior and Angular Dispersion

From the results in subsection 6.1, it is evident, that the ghosts exhibit dispersive behavior. A clear offset in the positions of the ghost peaks was observed, with the position dependent on the wavelength. In contrast, the position of the main peak (the BS) remained consistent across color bands.

The angular dispersion shows that shorter wavelengths are deflected at smaller angles compared to longer wavelengths in the R band. This pattern is symmetrical for each ghost, with shorter wavelengths positioned closer to the main peak and longer wavelengths further away, consistent with diffraction behavior. This observation contrasts with the normal dispersion expected from refraction in optical elements unless the case involves anomalous dispersion, where the refractive index increases with increasing wavelength. Meanwhile, internal reflections within the camera lens could potentially cause the observed chromatic aberrations of the ghosts. Due to limited information about the lens design, the origin of this effect remains unclear. A detailed analysis of the lens design, including the influence of Extra-Low Dispersion (ED) elements and their potential reverse chromatism to reduce chromatic aberrations, would be necessary for further insights.

The placement of the ghosts was symmetrical around the main peak with similar intensities. The relative intensity was highest for the shorter wavelengths in the blue band, despite the green band showing the highest measured intensity for the main peak. This behavior is also consistent with expectations for a diffraction grating, where the intensity depends on the diffraction angle. Longer wavelengths are diffracted more, resulting in greater separation and a broader distribution of light.

7.2 Symmetry and Intensity of Ghosts

The observed symmetry and equal relative intensities of the ghosts suggest they are not reflections of different orders, as such reflections would result in noticeable differences in intensity and focus. The innermost ghost exhibited a broader peak width, potentially due to interference from the earthshine-illuminated surface of the Moon or uneven placement of the intensity profile.

If the ghosts originated solely from window reflections, they would likely appear on one side of the BS and exhibit asymmetry. Their focused appearance and similarity to the main image suggest they are formed within the imaging part of the optical system, possibly involving the lens or sensor.
The windows may contribute to the overall optical system's complexity. Anti-reflective coat-

ings on the windows are less effective at non-normal incidence angles, allowing reflections to occur at angles exceeding 30°. Scratches or warping in the panes could degrade optical quality and introduce stray light. However, window reflections alone are unlikely to account for the observed symmetrical ghosting.

7.3   Potential Sources of Ghosting

From Figure 10, the angular dispersion derived from the ghost positions is similar to the theoretical behavior of a diffraction grating with slit widths equal to the pixel pitch. However, this result is an approximation, as it relies on assumptions about the wavelengths associated with each color band. The exact spectral response of the Nikon D5 sensor is unknown, and each color band covers a broad wavelength range, with the green filter typically encompassing parts of both the blue and red ranges.

Furthermore, the calculated distance between the sensor and the reflective element is based on mean values from estimated angles, which may not represent the actual setup. This introduces potential biases, as the analysis assumes the sensor itself causes the diffraction, neglecting alternative explanations for the reflections.

The measured angular dispersion of the ghosts aligns with the theoretical behavior of a one-dimensional diffraction. However, the Nikon D5 sensor's design includes gapless microlenses and lacks a repeating one-dimensional pattern, making diffraction from the sensor an unlikely source. If the sensor were responsible, a two-dimensional diffraction grating pattern would be expected, producing four first-order ghosts rather than the observed symmetrical pair.

If the sensor is not responsible, other components of the optical system must be considered. Internal reflections within the lens could generate the ghosting effect, particularly given the brightness of the Moon against the dark sky. The telephoto lens comprises multiple elements, each of which could contribute to internal reflections.

The possibility of the windows of Cupola as the source is also considered. While the windows are unlikely to contain a diffraction grating, they have reduced optical quality due to impacts from space debris and scratches on the innermost pane. Andreas Mogensen also addressed this issue and added "Dust is present between windows layers, which cannot be removed".

7.4   Ray Tracing Simulations

Ray tracing simulations using Zemax revealed minor stray light from the Cupola windows but failed to reproduce the observed ghost pattern. The simplified model excluded the lens and camera, key components in understanding interactions within the optical system. Additionally, the simulation did not account for potential warping or misalignment of window surfaces, which may influence the observed pattern. To address this, future work would include more realistic models that include a mockup of the telephoto lens including the camera sensor and the windows of cupola to simulate the actual setup. Simulations should also consider possible non-parallel surfaces in the window systems and deformation at different panes. Further

enhanced models could also include the filter stack (IR cut filter) non-parallel to the sensor surface and permitting reflections at the sensor.

The symmetrical displacement of the ghosts suggests a complex interplay of reflections and diffraction. Multiple reflections involving both the windows and lens are plausible but require further modeling to confirm.

7.5 Methodological Limitations

The accuracy of the profile measurements was constrained by the placement of the ghosts relative to the BS. Uneven intersections limited the ability to measure equivalent areas for each object within a single profile, reducing the reliability of intensity comparisons.
Significant noise in the images also affected measurements. While averaging improved the signal-to-noise ratio (SNR), it was limited to six images to preserve consistency in ghost positions. Further, underexposure was not adequately addressed, and electronic noise reduction was restricted to median filtering.
A higher bit-depth would have provided better contrast than the 12-bit data used. The Nikon D5 is capable of recording the images as uint14. Dark frame subtraction could also have effectively reduced noise, improving measurement accuracy.

To summarize, the analysis revealed angular dispersion in the ghosts, consistent with diffraction. However, the symmetrical pattern and relative intensities suggest a more complex mechanism involving internal reflections or diffraction within the optical system. The Cupola windows and telephoto lens are plausible contributors, but no definitive source was identified. The ray tracing simulations lacked critical components and could not replicate the observed pattern. Further investigation into the sensor design, lens elements, and window properties is necessary to clarify the ghosting mechanism. By addressing the methodological limitations and improving simulations, future studies could better determine the origin of these artifacts and their impact on the Earthshine experiment.

8   Future Work

Based on the findings and limitations of the investigation, future work would include:

Expanded Image Analysis

- Examine ghost patterns in additional datasets, such as Group 2 images described in section 4 or those captured by NASA astronaut Matthew Dominick, to analyze angular dispersion and higher-order ghosting effects.

- Optimize the placement of profiles to measure equivalent areas for each object and improve intensity comparisons.

Removal of Ghosts By Image Processing

- Develop methods to subtract ghost artifacts based on their observed characteristics, using templates to identify and remove ghost signals.

Improved Simulations

- Perform ray tracing with accurate models of the full optical system, including lens and camera components, to analyze stray light and internal reflections.

- Recreate the experimental setup to validate findings and identify interactions between the lens and Cupola windows

Lens and Window Analysis

- Investigate the optical properties of the Cupola windows, including potential diffraction or dispersive effects.

- Evaluate alternative lenses or camera systems with reduced ghosting for similar experiments. This could be investigated by using shorter lenses compatible with the Nikon D5 camera, shorter lenses also consist of fewer elements which minimizes the amount of possible reflections at each surface. Furthermore, shorter lenses enable a larger distance between the camera and the windows.

Improvement of Experimental Setup

- Enhance experimental design to mitigate ghost artifacts and better understand their impact on the halo profile in the Earthshine experiment. As mentioned above, experiments with different types of lenses could minimize the amount of stray light and ghosting in

the images. In addition, a polarizing filter could be implemented to investigate the effect on the ghosts.

- Change experimental setup to reduce the incident angle at the windows and ensure parallel surfaces in the optical system. The experiment could also be conducted outside of the ISS on potential spacewalks to rule out the cupola windows as the cause of the ghosts.

9   Conclusion

This study investigated the characteristics of ghosts observed in the images from the Earthshine experiment, aiming to identify their origin within the optical system and evaluate the impact on the halo profile. By understanding the dispersive behavior of these artifacts, the study sought to inform potential improvements in Earthshine observations from the International Space Station.

The findings revealed that the ghost reflections exhibit angular dispersion, with the displacement of the ghosts increasing symmetrically with wavelength. The positions of the ghosts, measured using color information from the RAW images, showed that the distances between the ghosts and the bright side of the Moon increased with wavelength. The position of the main image remained constant across all color bands, and the relative intensities of the two ghosts displayed symmetry. These results are consistent with the behavior of a one-dimensional diffraction grating.

Despite these insights, the specific source of the ghost reflections remains unclear due to insufficient information about the optical components and camera sensor design. Additionally, the method's accuracy was constrained by the proximity of the ghosts to the main image, limiting the ability to measure comparable areas and affecting the precision of the comparisons.

Ray-tracing simulations of a similar optical setup provided some insights into stray light produced by the Cupola windows but failed to replicate the observed ghosting patterns. This suggests that the ghosts may arise from optical elements or interactions not fully captured in the simulation.

Future work would include: Improved measurement techniques by developing enhanced methods, for extracting pixel intensity profiles to facilitate more accurate comparisons of the ghosts and the main image. Removal of the ghost artifacts, by image processing techniques to find and subtract the ghosts based on their wavelength-dependent characteristics, as identified in this study. Lastly, investigate the source of the ghosts by recreating the original experimental setup or conducting detailed ray-tracing simulations. These simulations should incorporate accurate models of the entire optical system, including the camera sensor, lens design, and any additional components, to better estimate the origin of the reflections.

In conclusion, the analysis of the ghost artifacts of the Moon images demonstrated clear wavelength-dependent behavior resembling angular dispersion caused by a diffraction grating. These findings provide valuable insights for estimating the distortion of halo profiles in the Earthshine experiment and offer a foundation for developing methods to mitigate ghost artifacts in future analyses.

Bibliography

[1]   ESA. *Illuminating Earth's shine*. Accessed 31th May 2024. URL:
       `https://www.esa.int/Science_Exploration/Human_and_Robotic_Exploration/`
       `Illuminating_Earth_s_shine`.

[2]   Rasmus Reinhold Paulsen and Thomas B. Moeslund. *Introduction to Medical Image
       Analysis*. English. 1. Undergraduate Topics in Computer Science. Germany: Springer,
       2020. ISBN: 978-3-030-39363-2. DOI: `10.1007/978-3-030-39364-9`.

[3]   José Sasián. *Introduction to Lens Design*. Cambridge University Press, 2019.

[4]   Mathilde Saltoft Schou. "Analysis of Andreas Mogensen's moon images: a DTU
       Bachelor's Thesis". In: 2024. URL:
       `https://www.dmi.dk/fileadmin/Rapporter/2024/DMI_rapport_24_13.pdf`.

[5]   Dave Etchells. *Pixels for Geeks: A peek inside Nikon's super-secret sensor design lab*.
       Accessed 11th December 2024. URL:
       `https://www.imaging-resource.com/news/2018/07/17/pixels-for-geeks-a-peek-`
       `inside-nikons-super-secret-sensor-design-lab`.

[6]   Nikon. *What is an Optical Low Pass Filter?* Accessed 18th December 2024. URL:
       `https://www.nikonimgsupport.com/eu/BV_article?articleNo=000044799&`
       `configured=1&lang=en_GB`.

[7]   Johannes Brauers and Til Aach. "Ghosting Reflection Compensation for Multispectral
       High Dynamic Range Imaging". In: *Color and Imaging Conference* 17.1 (2009),
       pp. 170–170. DOI: `10.2352/CIC.2009.17.1.art00032`. URL:
       `https://library.imaging.org/cic/articles/17/1/art00032`.

[8]   Frank L. Pedrotti, Leno M. Pedrotti, and Leno S. Pedrotti. *Introduction to Optics*. 3rd ed.
       Cambridge University Press, 2017.

[9]   ESA. "Annex 1: Additional technical Information on ISS capabilities and background
       information". In: 2010.

[10]   Digital Photography Review. *Nikon AF-S Nikkor 400mm f/2.8D ED-IF II Specs*. Accessed
       9th December 2024. URL: `https:`
       `//www.dpreview.com/products/nikon/lenses/nikon_400_2p8d_ii/specifications`.

[11]   Nikon. *NIKKOR Lens Glossary*. Accessed 9th December 2024. URL:
       `https://imaging.nikon.com/imaging/lineup/lens/glossary/`.

[12]   *About LibRaw*. Accessed 30th May 2024. URL: `https://www.libraw.org/`.

[13]   Pauli Virtanen et al. "SciPy 1.0: Fundamental Algorithms for Scientific Computing in
       Python". In: *Nature Methods* 17 (2020), pp. 261–272. DOI: `10.1038/s41592-019-0686-2`.

[14]   Orit Skorka, Paul Kane, and Radu Ispasoiu. "Color correction for RGB sensors with
       dual-band filters for in-cabin imaging applications". In: *Electronic Imaging* 2019 (Jan.
       2019), pp. 46–1. DOI: `10.2352/ISSN.2470-1173.2019.15.AVM-046`.

A Appendix

A.1 Ghost Observations - Appendix

iss071e160726.NEF | 2024:06:03 13:59:39

Figure 13: Image taken by the NASA astronaut Matthew Dominick as a part of the extended earthshine experiment.

A.2 Angular Profile

A.2.1 Output

```
Angular profile GMT009
B Detected peaks at indices: [ 73 106 135]
B Peak heights: [   9.36570084 1754.57107796   10.68808993]
B Main peak at position 106.66, intensity 1754.57
B Ghost peaks at positions 73.46, 135.85
B Distance Ghost 1 = 33.21, Ghost 2 = 29.18

G Detected peaks at indices: [ 67 106 138]
G Peak heights: [   13.17792614 2925.77389408   12.92890599]
G Main peak at position 106.66, intensity 2925.77
G Ghost peaks at positions 67.42, 138.86
G Distance Ghost 1 = 39.24, Ghost 2 = 32.20

G2 Detected peaks at indices: [ 68 106 139]
G2 Peak heights: [   11.69784621 2894.47283405   13.33994167]
G2 Main peak at position 106.66, intensity 2894.47
G2 Ghost peaks at positions 68.43, 139.87
G2 Distance Ghost 1 = 38.24, Ghost 2 = 33.21

R Detected peaks at indices: [ 63 106 142]
R Peak heights: [   4.69311991 1442.69737904    4.88541762]
R Main peak at position 106.66, intensity 1442.70
R Ghost peaks at positions 63.39, 142.89
R Distance Ghost 1 = 43.27, Ghost 2 = 36.23
```

A.2.2 Normalized Porfiles

```
Theoretical vs measured B
inner Ghost B angle is -4.49931212263772
Theoretical inner Ghost B angle is -4.025635924290187
Theoretical inner Ghost B distance is -29.698640273473806
Measured inner Ghost B distance is -33.20677696630395

Outer Ghost B angle is 3.955791117546862
Theoretical outer Ghost B angle is 4.025635924290187
Theoretical outer Ghost B distance is 29.698640273473806
Measured inner Ghost B distance is 29.18171309160043
```

```
Theoretical vs measured G
inner Ghost G angle is -5.3130446597126895
Theoretical inner Ghost G angle is -4.87737051578696
Theoretical inner Ghost G distance is -36.010003767651014
Measured inner Ghost G distance is -39.24437277835921

Outer Ghost G angle is 4.363504084353328
Theoretical outer Ghost G angle is 4.87737051578696
Theoretical outer Ghost G distance is 36.010003767651014
Measured inner Ghost G distance is 32.20051099762806


Theoretical vs measured G2
inner Ghost G2 angle is -5.177562830645371
Theoretical inner Ghost G2 angle is -4.87737051578696
Theoretical inner Ghost G2 distance is -36.010003767651014
Measured inner Ghost G2 distance is -38.23810680968333

Outer Ghost G2 angle is 4.499312122637718
Theoretical outer Ghost G2 angle is 4.87737051578696
Theoretical outer Ghost G2 distance is 36.010003767651014
Measured inner Ghost G2 distance is 33.206776966303934


Theoretical vs measured R
inner Ghost R angle is -5.854361680691524
Theoretical inner Ghost R angle is -5.595451967827915
Theoretical inner Ghost R distance is -41.343336737425425
Measured inner Ghost R distance is -43.26943665306271

Outer Ghost R angle is 4.906426406961263
Theoretical outer Ghost R angle is 5.595451967827915
Theoretical outer Ghost R distance is 41.343336737425425
Measured inner Ghost R distance is 36.22557487233156
```
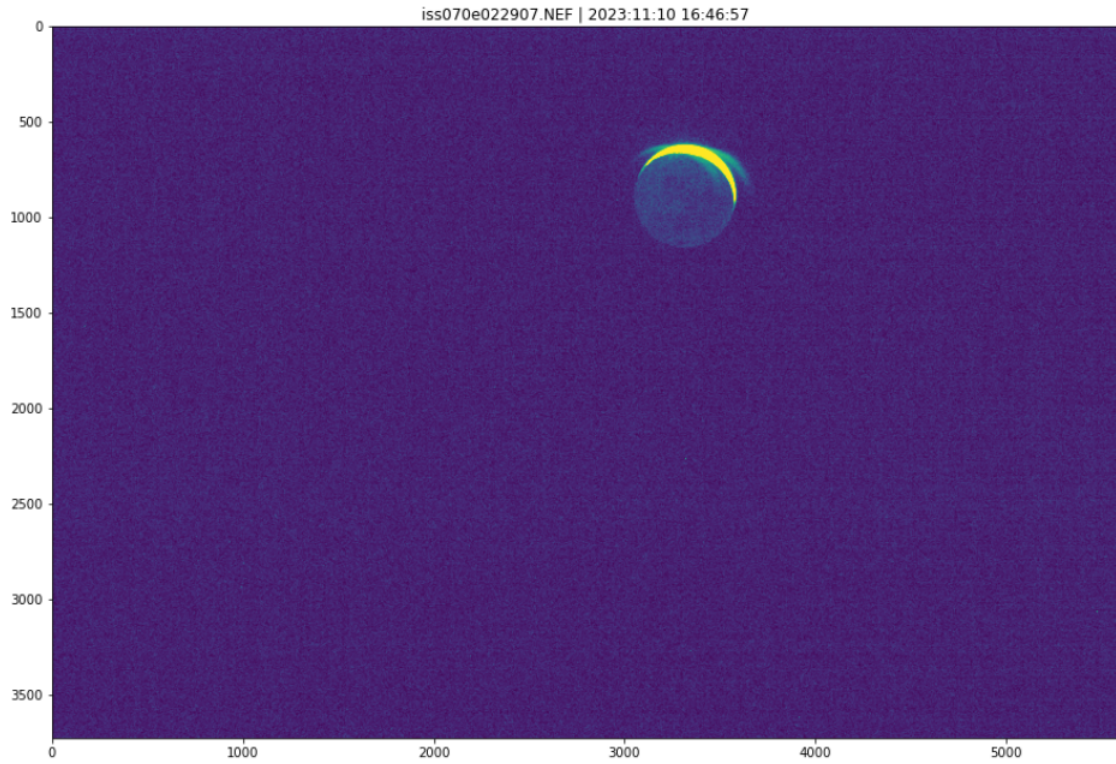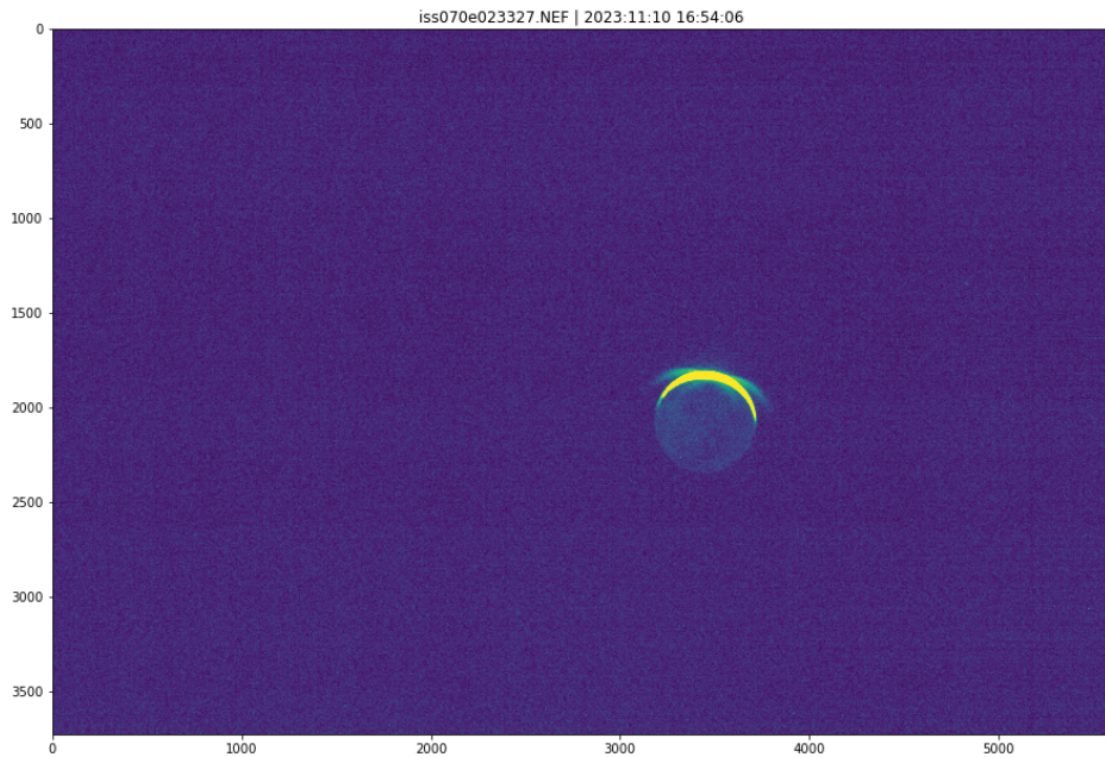
A.3 Zemax

iss070e022907.NEF | 2023:11:10 16:46:57

(a) iss070e023327.NEF at 16:46:57

iss070e023327.NEF | 2023:11:10 16:54:06

(b) iss070e023327.NEF at 16:54:06

Figure 14: Change in the pattern within a series of images, the images are taken 7 min apart.
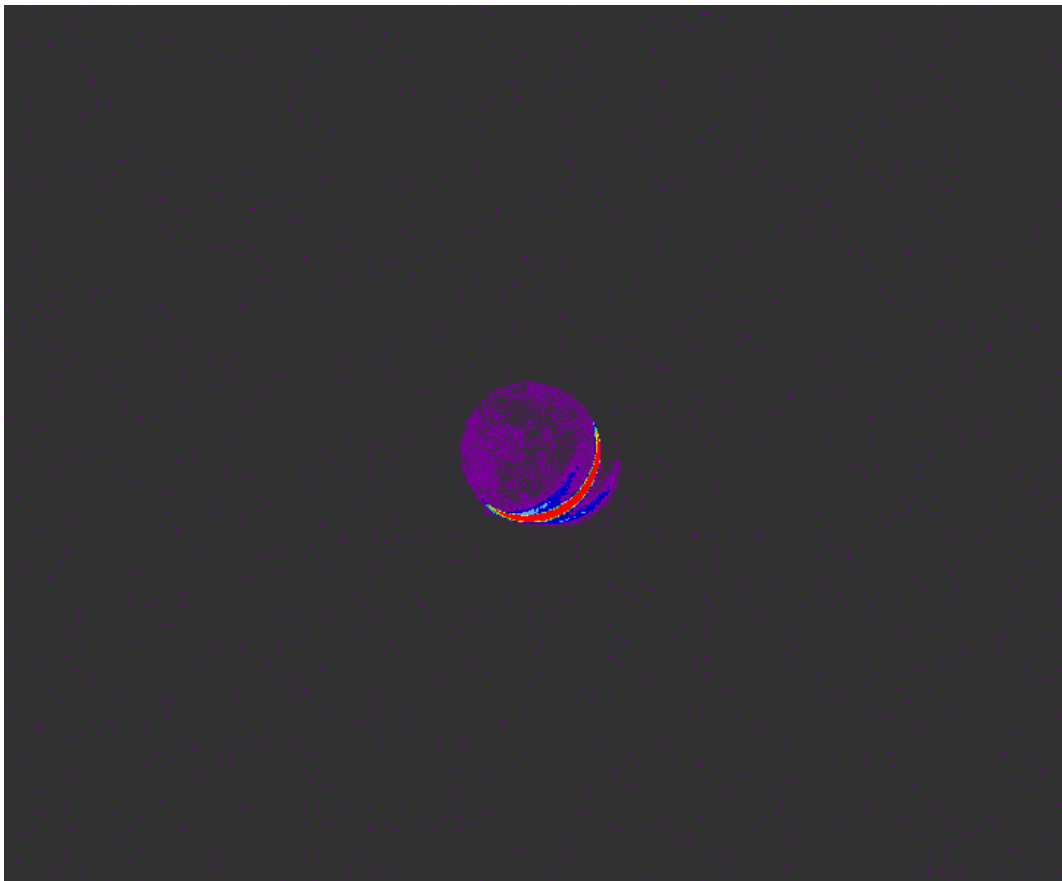
Figure 15: GMT009 average image in the G2 color band

(a) R Normalized Intensity Profile

(b) G Normalized Intensity Profile

(c) G2 Normalized Intensity Profile
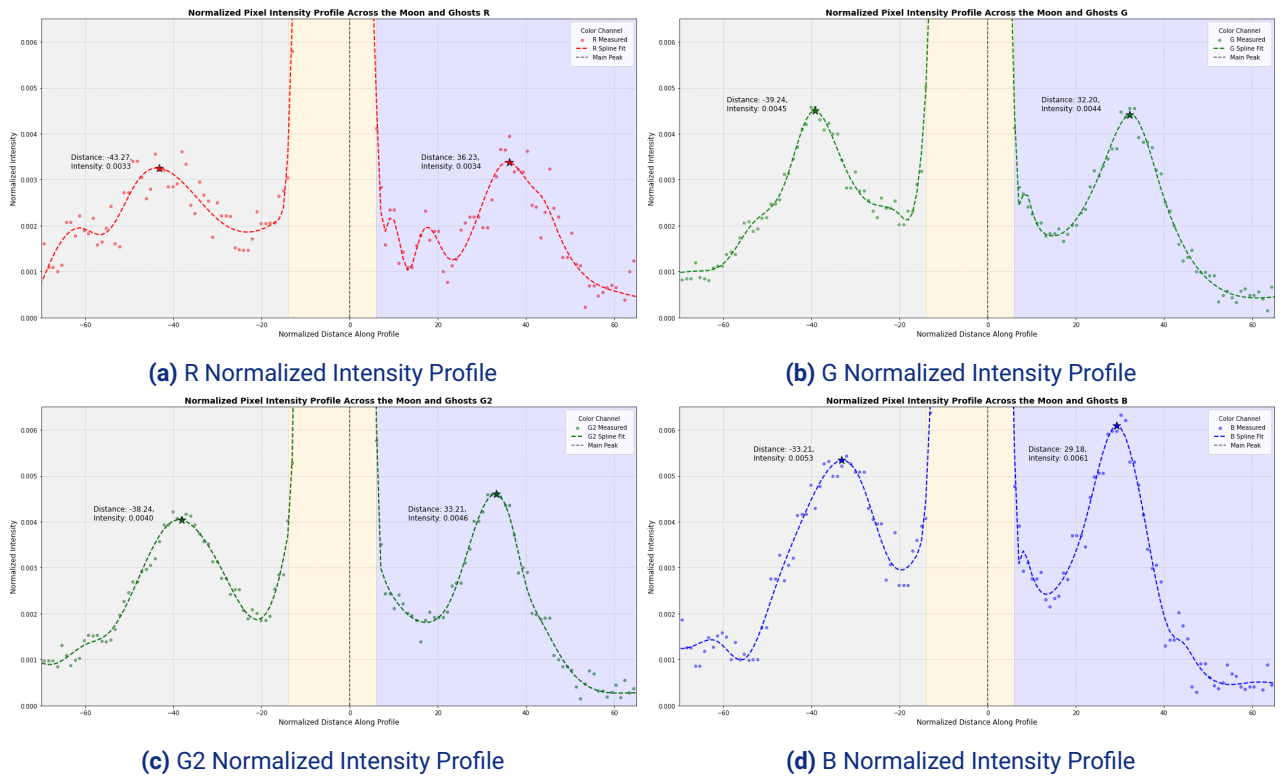

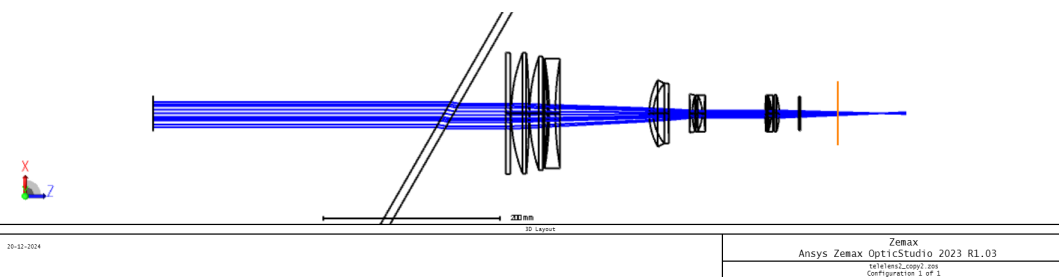**(d)** B Normalized Intensity Profile

Figure 16

Figure 17: an attempt was made to recreate the Nikon Nikkor 400mm f/2.8D AF-S ED-IF II